Chemical Science

ROYAL SOCIETY OF CHEMISTRY

EDGE ARTICLE

View Article Online
View Journal | View Issue

Cite this: *Chem. Sci.*, 2025, **16**, 4668

All publication charges for this article have been paid for by the Royal Society of Chemistry

Received 27th November 2024
Accepted 29th January 2025

DOI: 10.1039/d4sc08026b

rsc.li/chemical-science

Stable luminescent diphenylamine biphenylmethyl radicals with α-type $D_0 \rightarrow D_1$ transition and antiferromagnetic properties†

Shengxiang Gao, Chunxiao Wu, Ming Zhang and Feng Li *

Organic luminescent radicals, with their open-shell electronic structure, exhibit appealing optoelectronic properties and hold promise for a wide range of potential applications. Although a few series of luminescent radicals have been reported, most feature $D_0 \rightarrow D_1$ transitions dominated by HOMOβ–SOMOβ (β-type transitions). In contrast, luminescent radicals that exhibit SOMOα–LUMOα properties (α-type transitions) are much rarer. Here, we designed and synthesized two stable novel diphenylamine biphenylmethyl (BTM) luminescent radicals, both characterized by α-type $D_0 \rightarrow D_1$ transitions, and simultaneously maintained the D–A$^{\bullet}$ structure for the first time. Density functional theory (DFT) calculations confirmed that fine-tuning the energy levels of frontier molecular orbitals can facilitate β-type to α-type $D_0 \rightarrow D_1$ transition. Besides, in a **2(2Cl(m)PhN)-BTM** crystal we for the first time observed strong antiferromagnetic interactions among luminescent radicals through SQUID measurements. This work offers design insights into luminescent radicals with α-type transition for future development.

Introduction

Organic luminescent radicals, characterized by their unique photo-electro-magnetic properties, have found widespread application in various research fields. Particularly noteworthy is their potential use in organic light-emitting diodes (OLEDs), where the spin-allowed doublet transition theoretically enables an internal quantum efficiency (IQE) approaching 100%.[1–7] Most of the stable organic luminescent radicals reported to date fall within the category of chlorinated triphenylmethyl carbon radicals and their derivatives. These primarily include perchlorotriphenyl methyl radical derivatives (**PTM**),[8–10] tris(2,4,6-trichlorophenyl)methyl radical derivatives (**TTM**),[11–14] and pyridyl-containing triarylmethyl radicals (**Py-BTM**)[15–18] and their derivatives. Besides, our group reported an (*N*-carbazolyl) bis(2,4,6-trichlorophenyl)-methyl radical (**Cz-BTM**)[19] and a similar (*N*-pyrido[3,4-*b*]indolyl)bis(2,4,6-trichlorophenyl) methyl radical (**PyID-BTM**),[20] in which the central carbon atoms of the radicals are directly bonded to nitrogen atoms. However, compared to the extensively studied **TTM**, **PTM**, and **Py-BTM** radical derivatives, **Cz-BTM** derivatives have received considerably less attention in the literature and with very limited reported derivatives.

In open-shell molecules, the presence of unpaired electrons causes all molecular orbitals to split into two sub-orbitals, α and β, each with opposite electron spins. Consequently, the transition to the first excited state ($D_0 \rightarrow D_1$) of radicals can follow two possible excitation pathways: excitation of the unpaired electron from SOMOα to LUMOα, known as the α-type transition, or from HOMOβ to SOMOβ, known as the β-type transition (Scheme 1a).[21–23] The luminescence process is the reverse of the corresponding excitation pathway. Currently, the most effective strategy for enhancing the stability and luminescence efficiency of luminescent radicals involves modifying the molecule with various electron donors to form donor–acceptor radicals (D–A$^{\bullet}$). As a result, their first excited states typically exhibit significant charge transfer (CT) properties, with the electron primarily transitioning from HOMOβ (where the electron cloud is concentrated on the donor) to SOMOβ (where the electron cloud is concentrated on the radical), thus following the β-type transition pathway. Nearly all reported D–A type luminescent radicals exhibit β-type transitions. The luminescent radicals with α-type transitions reported are very rare, due to the highly complex design and synthesis which hinders further development and exploration.[24,25] α-Type transition luminescent radicals have distinctive potential in researching new efficient luminescent radical systems and developing applications. For instance, in OLEDs some host materials with a shallower HOMO energy level can be used because of the shallower energy levels of SOMOα/LUMOα than those of HOMOβ/SOMOβ in radicals, which has the potential to expand the selection range of host materials. Developing α-type transition luminescent radicals with straightforward design and synthesis is also

State Key Laboratory of Supramolecular Structure and Materials, College of Chemistry, Jilin University, Qianjin Avenue 2699, Changchun, 130012, China. E-mail: lifeng01@jlu.edu.cn

† Electronic supplementary information (ESI) available. CCDC 2384400 and 2384389. For ESI and crystallographic data in CIF or other electronic format see DOI: https://doi.org/10.1039/d4sc08026b

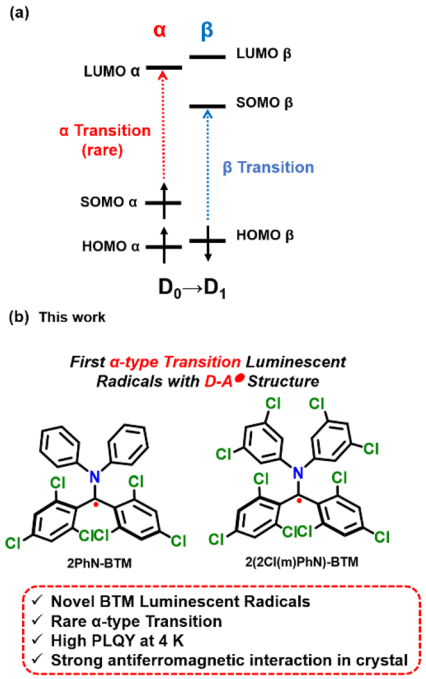

Scheme 1 (a) Schematic representation of α and β transitions. (b) Structures of the stable luminescent diphenylamine biphenylmethyl radicals in this study.

pivotal for broadening the diversity of radical luminescence, advancing the understanding of luminescence mechanisms, and gaining deeper insights into the photophysical processes involved.

In this work, we designed and synthesized two novel diphenylamine BTM luminescent radicals: (*N*-diphenylamine) bis(2,4,6-trichlorophenyl)methyl radical (**2PhN-BTM**) and (*N*-bis(3,5-dichlorophenyl)amine)bis(2,4,6-trichlorophenyl)methyl radical (**2(2Cl(m)PhN)-BTM**) (Scheme 1b). Theoretical calculations reveal that both **2PhN-BTM** and **2(2Cl(m)PhN)-BTM** exhibit α-type $D_0 \rightarrow D_1$ transition, but maintain the radical moieties functioning as electron acceptors. Therefore, these novel diphenylamine BTM luminescent radicals are also the first α-type transition luminescent radicals with D–A˙ structure, which is distinct from previous α-type transition luminescent radicals where the radical moiety acts as an electron donor. This not only broadens the BTM luminescent radical system, but also confirms the simple design strategy by fine-tuning the energy levels of frontier molecular orbitals for developing luminescent radicals with α-type transition.

Experimental

Materials

All starting materials were obtained from commercial suppliers and used without further purification. The intermediate **HBTM-Br** and biphenylmethyl radicals were prepared by a previously reported method.[19,20] Detailed synthesis procedures and characterization results are provided in the ESI.†

Characterization

GC-MS mass spectra were recorded on a Thermo Fisher ITQ1100 mass spectrometer. The ^{1}H and ^{13}C nuclear magnetic resonance (NMR) spectra were recorded in a solution of $CDCl_3$ on a Bruker AVANCEIII500 NMR spectrometer with TMS as the internal standard. Elemental analysis data were recorded on a Elementar Vario micro cube. EPR spectra were recorded on a Bruker ELEXSYSII E500 CW-EPR spectrometer in the ambient atmosphere. All photophysical measurements were performed in cyclohexane solution around 10^{-5} M at room temperature. A UV/Vis spectrophotometer (Shimadzu UV-2550) and spectrofluoro-photometer (Shimadzu RF-6000) were used to measure the absorption and fluorescence spectra in solution respectively. Single crystal X-ray diffraction data were collected on a Bruker Apex II CCD diffractometer at 293(2) K. The CV measurements were performed using an electrochemical analyzer (CHI660C, CH Instruments, USA) at the rate of 100 mV s^{-1}. A glass carbon disk was used as the working electrode and a platinum wire acted as the counter electrode and Ag/AgCl acted as the reference electrode. Tetrabutylammonium hexafluorophosphate ($TBAPF_6$) in anhydrous dichloromethane was used as the supporting electrolyte. The photoluminescence decay spectra measurements were carried out on Edinburgh Instruments spectrometer FLS980-S2S2-stm. Magnetic measurements were performed on a Quantum Design MPMS3-Zxin system with a temperature range of 1.9–300 K and an applied field of 0.5 T. The polycrystalline samples were prepared by a solvent evaporation method, ground and air dried. The amount used for testing was 0.03 mmol. The data were corrected for diamagnetism of the sample holder.

Computational methods

DFT calculations were performed on a Gaussian09 series of programs using the (U)B3LYP function and 6-31G(d,p) basis, and using cyclohexane as the solvent in all calculations.[26] Hole–electron analysis was performed on Multiwfn 3.8 program.[27,28]

Results and discussion

Synthesis and characterization

The synthesis of diphenylamine BTM radicals follows a similar pathway to that of the reported **Cz/PyID-BTM** radicals, utilizing a one-step reaction of diphenylamine derivatives with the intermediate **HBTM-Br**, as depicted in the ESI.† Consistent with **Cz-BTM** radical derivatives, both diphenylamine BTM radicals exhibit robust stability in the presence of oxygen, water, and light. They remain stable both as solids and in solution over extended periods under ambient conditions.

EPR spectroscopy of **2PhN-BTM** (Fig. 1a) confirmed the existence of an unpaired electron with $g = 2.0038$. The molecular structure in crystalline form was analyzed by single crystal X-ray diffraction (Table S1†). The single crystal of **2PhN-BTM** was obtained through evaporation of cyclohexane/dichloromethane solution. The radical center atom, C23, is sterically shielded by four benzene rings and is coplanar with the adjacent N1, C2, and C7 atoms, confirming the sp^2

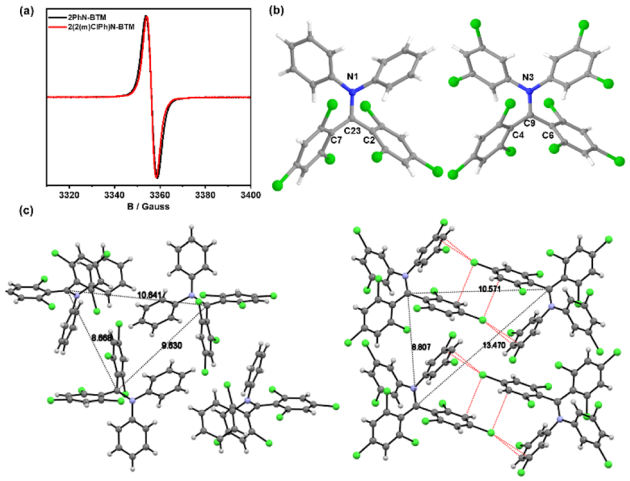

Fig. 1 (a) EPR spectrum of **2PhN-BTM** and **2(2Cl(m)PhN)-BTM** in DCM solution (10^{-3} M) at room temperature. (b) Crystal structure of **2PhN-BTM** and **2(2Cl(m)PhN)-BTM**. (c) The crystal stacking structure of **2PhN-BTM** and **2(2Cl(m)PhN)-BTM**; black dashed lines: the distance between the central carbon atoms of adjacent radicals; red dashed lines: Cl···π halogen bonds between adjacent **2(2Cl(m)PhN)-BTM** molecules.

hybridization of the radical center (Fig. 1b). However, significant decomposition was observed during the purification of **2PhN-BTM** using silica gel column chromatography, resulting in a reduction in yield. This decomposition was partially mitigated by employing alumina column chromatography.

To enhance the stability of diphenylamine BTM radicals during purification, we explored incorporating chlorine atoms that are commonly used to stabilize triphenylmethyl radicals onto the benzene rings of diphenylamine. Despite the extensive steric hindrance provided by bis(2,4,6-trichlorophenyl)amine, this compound did not react with **HBTM-Br** to form the target radicals due to the increased activation energy caused by the substantial steric hindrance. Consequently, we modified the chlorine atoms to the meta-positions and successfully synthesized the target radical **2(2Cl(m)PhN)-BTM** by reacting bis(3,5-dichlorophenyl)amine with **HBTM-Br**. This modification significantly improved the stability of **2(2Cl(m)PhN)-BTM** during column chromatography, resulting in nearly complete avoidance of decomposition and a marked increase in yield. The purities of **2PhN-BTM** (94%) and **2(2Cl(m)PhN)-BTM** (95%) were determined *via* EPR measurements, employing 10^{-4} M TEMPO in toluene as an internal standard.

As shown in Fig. 1a, the EPR signal ($g = 2.0038$) of **2(2Cl(m)PhN)-BTM** was similar to that of **2PhN-BTM**. Due to the increased chlorine content reducing solubility in low-polarity solvents, single crystals were obtained by evaporation of tetrahydrofuran/acetonitrile solution. In the **2(2Cl(m)PhN)-BTM** crystal, the radical center atom C9 is coplanar with N3, C4 and C6 atoms (Fig. 1b). The intermolecular distance between **2PhN-BTM** molecules (measured from the central carbon atom) is 8.668 Å, 9.630 Å and 10.641 Å (Fig. 1c). For **2(2Cl(m)PhN)-BTM**, these distances increase to 8.807 Å, 10.571 Å and 13.470 Å, indicating that the chlorine atoms on the benzene rings of diphenylamine provide steric hindrance effectively, protecting the radical center. In addition, **2(2Cl(m)PhN)-BTM** presents multiple Cl···π halogen bonds between adjacent molecules in the crystal (Fig. 1c). This characteristic affects the magnetic properties of **2(2Cl(m)PhN)-BTM** at low temperatures (see below). Moreover, the electron-withdrawing nature of the chlorine atoms enhances stability by lowering the energy levels of the frontier orbitals. Cyclic voltammetry (CV) measurements of **2PhN-BTM** (Fig. S2†) suggest that SOMOα and SOMOβ energy levels are at −4.50 eV and −3.42 eV, respectively, whereas for **2(2Cl(m)PhN)-BTM**, these values are at −4.86 eV and −3.64 eV. This reduction in SOMO energy levels confirms that the chlorine atoms effectively lower the energy levels of the frontier orbitals, thereby reducing reactivity and improving stability.

Photophysical properties

Fig. 2a presents the UV/Vis absorption spectra of **2PhN-BTM** and **2(2Cl(m)PhN)-BTM** in cyclohexane. In the long-wavelength region (wavelengths > 450 nm), both compounds exhibit characteristic absorption peaks attributed primarily to transitions in the frontier orbitals. **2PhN-BTM** exhibits two closely positioned absorption peaks at 506 nm and 579 nm. Time-dependent density functional theory (TD-DFT) calculations (UB3LYP, 6-31G(d,p)) assign these peaks to $D_0 \rightarrow D_2$ and $D_0 \rightarrow D_1$ excitations, respectively (Table S2†). The difference in peak intensities aligns with calculation predicted oscillator strengths. Notably, the $D_0 \rightarrow D_1$ excitation process in **2PhN-BTM** involves transitions predominantly from the SOMOα orbital (137α) to the LUMOα orbital (138α), contributing over 94% to the excitation, indicative of an α-type transition. This contrasts with traditional D–A˙ type luminescent radicals, where the first excited states

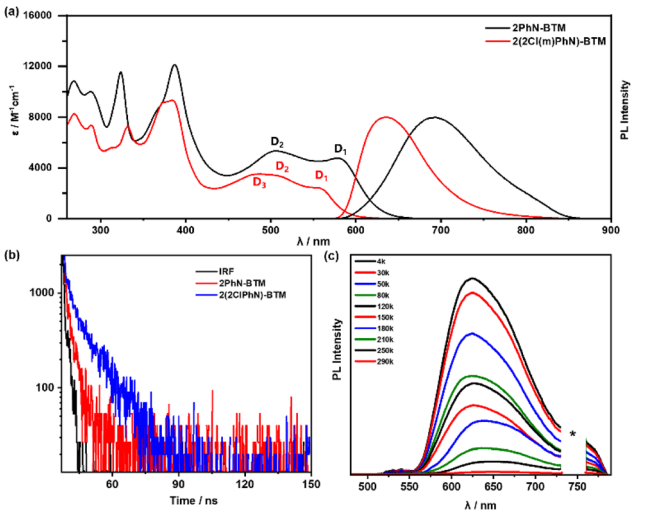

Fig. 2 (a) Absorption and emission spectra of **2PhN-BTM** and **2(2Cl(m)PhN)-BTM** in cyclohexane solution (10^{-5} M) under excitation at 365 nm at room temperature. (b) Photoluminescence decay spectra of **2PhN-BTM** and **2(2Cl(m)PhN)-BTM** in cyclohexane solution (10^{-5} M) under excitation at 365 nm at room temperature. (c) Photoluminescence spectra of **2(2Cl(m)PhN)-BTM** in cyclohexane solution at different temperatures under UV laser irradiation (365 nm) (the asterisk represents the harmonic peak of the light source).

typically involve HOMOβ–SOMOβ transitions (β-type transitions). The $D_0 \rightarrow D_2$ excitation in **2PhN-BTM** involves transitions from HOMOβ orbitals (136β) to SOMOβ orbitals (137β). Thus, the transition type of the first excited state is governed by the smaller energy gap between SOMOα–LUMOα and HOMOβ–SOMOβ. For **2(2Cl(m)PhN)-BTM**, three primary absorption peaks in the long-wavelength region are observed at 483 nm, 506 nm, and 556 nm. This corresponds to the SOMOα–LUMO+1α transition ($D_0 \rightarrow D_3$), the HOMOβ–SOMOβ transition ($D_0 \rightarrow D_2$), and the SOMOα–LUMOα transition ($D_0 \rightarrow D_1$), respectively. The absorption peak associated with the $D_0 \rightarrow D_1$ transition of **2(2Cl(m)PhN)-BTM** is slightly blue-shifted compared to **2PhN-BTM**, and due to lower oscillator strength, its molar extinction coefficient is also reduced.

In cyclohexane under 550 nm excitation, **2PhN-BTM** exhibits an emission band at 694 nm, comparable to that of the previously reported **Cz-BTM**. In contrast, **2(2Cl(m)PhN)-BTM** shows a notable blue shift of 58 nm to 636 nm. The alignment of the main absorption peaks with the excitation spectra confirms the origin of the emission (Fig. S3†). However, the PLQY of **2PhN-BTM** (0.14%) and **2(2Cl(m)PhN)-BTM** (0.27%) are significantly lower than that of **Cz-BTM** (2.0%) under 550 nm excitation in cyclohexane at room temperature. This reduced PLQY is likely attributed to the lack of connectivity between the *N*-benzene rings of diphenylamine compared to **Cz-BTM**. The unobstructed rotation of the benzene rings in both radicals facilitates non-radiative decay pathways. The transient photoluminescence decay measurements at room temperature (Fig. 2b) reveal that **2PhN-BTM** has a shorter lifetime (τ) of 3.14 ns compared to **2(2Cl(m)PhN)-BTM**, which has a lifetime of 8.27 ns. The radiative rate constants (k_r) and non-radiative rate constants (k_{nr}) were calculated from PLQY and τ values (Table S3†). **2(2Cl(m)PhN)-BTM** exhibits a significant reduction in k_{nr} compared to **2PhN-BTM**, attributed to the steric hindrance of chlorine atoms that restricts the rotation of the benzene rings. Reorganization energy (E_R) calculations for the excitation and de-excitation processes between D_0 and D_1 (Table S4†) indicate that **2(2Cl(m)PhN)-BTM** has lower semi-reorganization energy than **2PhN-BTM**, suggesting reduced non-radiative energy loss during the luminescence process. However, the k_r of **2(2Cl(m)PhN)-BTM** is lower than that of **2PhN-BTM**, primarily due to its lower oscillator strength for the first excited state. To investigate the impact of benzene ring rotation on the low PLQY, we measured the photoluminescence spectra of **2PhN-BTM** and **2(2Cl(m)PhN)-BTM** at reduced temperatures. As shown in Fig. S4,† the luminescence intensity of both compounds increased significantly at 80 K, with PLQYs rising to 1.5% and 8.6%, respectively. At 4 K, the PLQYs further increased to 2.6% and 16%, respectively (Fig. 2c and S5†). This substantial enhancement in PLQYs suggests that benzene ring rotation is effectively suppressed at low temperatures, thus reducing non-radiative transition rates.

We also evaluated the photo- and thermal stability of the compounds. Under 375 nm pulsed laser irradiation, both radicals presented much more enhanced photostability than the simplest luminescent radical **TTM** (Fig. S6†). **2PhN-BTM** presented a fitted half-life ($t_{1/2}$) of approximately 2.28×10^4 s, which is almost identical to that of **Cz-BTM** ($t_{1/2} = 2.13 \times 10^4$ s), attributed to their similar molecular structure. Interestingly, despite **2(2Cl(m)PhN)-BTM** showing enhanced stability during purification, **2PhN-BTM** exhibited superior photostability, whereas **2(2Cl(m)PhN)-BTM** displayed a shorter half-life ($t_{1/2} = 4.33 \times 10^3$ s), indicating reduced photostability. This decrease in photostability for **2(2Cl(m)PhN)-BTM** is likely due to the additional chlorine atoms.[29,30] The lower bond dissociation energy of the C–Cl bond (328 kJ mol^{-1}) compared to the C–H bond (414 kJ mol^{-1}) makes **2(2Cl(m)PhN)-BTM** more prone to photochemical degradation under UV exposure, attributed to the cleavage of the C–Cl bond. Thermogravimetric analysis (TGA) revealed that **2(2Cl(m)PhN)-BTM** exhibits slightly better thermal stability than **2PhN-BTM**, likely related to the lower energy level of its frontier molecular orbitals (Fig. S7†).

Theoretical calculations

We employed DFT calculations (UB3LYP, 6-31G(d,p)) to elucidate the energy levels and electron cloud distribution of frontier molecular orbitals in diphenylamine BTM radicals, aiming to understand the α-type transition mechanism (Fig. 3). For **Cz-BTM**, the β-type transition energy gap ($\Delta E_{HOMO\beta-SOMO\beta} = 3.0$ eV) is smaller than the α-type transition energy gap ($\Delta E_{SOMO\alpha-LUMO\alpha} = 3.53$ eV), making β-type transition the lowest energy excitation. For **2PhN-BTM**, diphenylamine raises the energy levels of both SOMOs and LUMOs. The rise of SOMO energy levels is more pronounced, reducing $\Delta E_{SOMO\alpha-LUMO\alpha}$ to 3.21 eV. Simultaneously, the SOMOβ energy level increases to −2.62 eV while the HOMOβ remains nearly unchanged, which widens the β-type transition gap to 3.38 eV, exceeding the α-type transition gap. Consequently, **2PhN-BTM** undergoes α-type transition. A similar pattern is observed in **2(2Cl(m)PhN)-BTM**, where the additional chlorine atoms significantly lower the frontier orbital energies. Compared to **Cz-BTM**, the LUMO energy levels in **2(2Cl(m)PhN)-BTM** are slightly reduced while the SOMO energy levels remain nearly unchanged. However, the HOMO energy levels decrease considerably. This results in a larger $\Delta E_{HOMO\beta-SOMO\beta}$ exceeding the $\Delta E_{SOMO\alpha-LUMO\alpha}$, which induces **2(2Cl(m)PhN)-BTM** to undergo α-type transition. The $\Delta E_{SOMO\alpha-LUMO\alpha}$ and $\Delta E_{HOMO\beta-SOMO\beta}$ for **2(2Cl(m)PhN)-BTM** are 3.44 eV and 3.53 eV, respectively; both are larger than those for **2PhN-BTM**, consistent with the observed blue shift of its absorption and emission spectra. Furthermore, the plane of one trichlorobenzene at the radical moiety is defined as the acceptor plane and the plane of carbazole or one diphenylamine benzene ring as the donor plane (Fig. 3). For **Cz-BTM**, the HOMO electron clouds primarily localize on the electron-donating moiety due to the large dihedral angle (77.72°) between the acceptor and donor planes, which hinders electron cloud delocalization from the carbazole to the radical moiety. In contrast, for **2PhN-BTM** and **2(2Cl(m)PhN)-BTM**, the rotation of diphenylamine benzene rings reduces the angle between the acceptor and donor planes (67.41° for **2PhN-BTM** and 66.70° for **2(2Cl(m)PhN)-BTM**). As a result, the HOMO electron clouds become more delocalized across the entire molecule. Therefore, by selecting electron-donating groups with appropriate donating

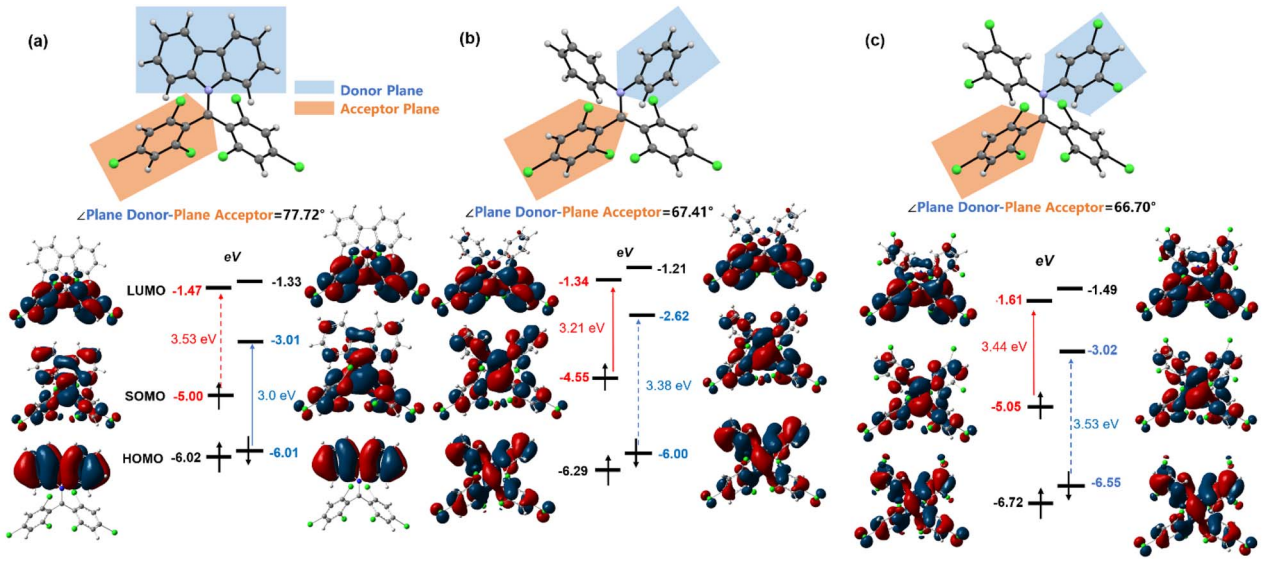

Fig. 3 Donor/acceptor plane angles and frontier orbitals of **Cz-BTM** (a), **2PhN-BTM** (b) and **2(2Cl(m)PhN)-BTM** (c) according to DFT calculations at the ground state (UB3LYP, 6-31G(d,p)) (isovalue = 0.02).

strengths and fine-tuning the molecular structure and orbital distribution, it is possible to modulate the α and β energy gaps and enable both α-type and β-type transitions of BTM radicals.

Although **2PhN-BTM** and **2(2Cl(m)PhN)-BTM** exhibit α-type transition of $D_0 \rightarrow D_1$, their charge transfer behavior remains similar to that of D–A˙ type luminescent radicals (for example, **Cz-BTM**). For **Cz-BTM**, upon excitation to the first excited state, the electron shifts from the carbazole moiety (HOMOβ orbital) to the entire molecule (SOMOβ orbital). For **2PhN-BTM**, however, the charge transfer occurs from the SOMOα orbital, where the electron cloud is delocalized across the entire molecule, to the LUMOα orbital, where the electron cloud is primarily localized on the radical moiety. For **2(2Cl(m)PhN)-BTM**, the electron-donating ability of the diphenylamine is

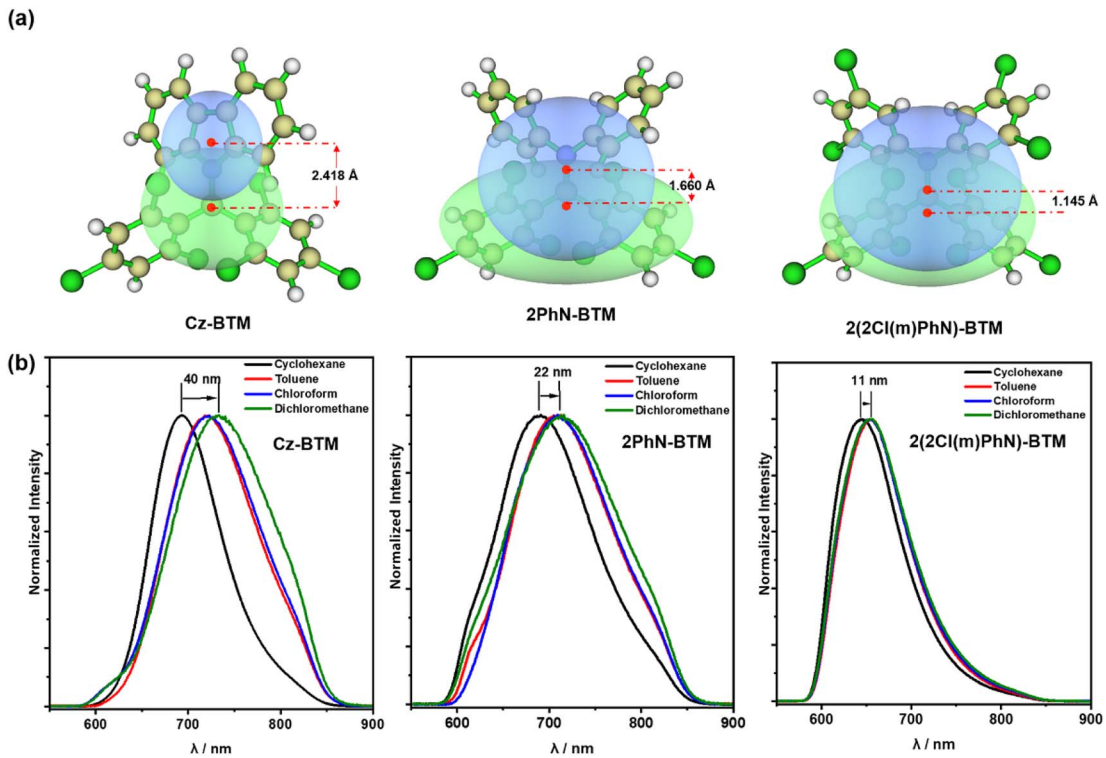

Fig. 4 (a) Hole(blue)–electron(green) analysis of **Cz-BTM**, **2PhN-BTM** and **2(2Cl(m)PhN)-BTM** for D0 → D1 transition and distance between the hole center and electron center. (b) Photoluminescence spectra of **Cz-BTM**, **2PhN-BTM** and **2(2Cl(m)PhN)-BTM** in different solutions under 375 nm irradiation at room temperature.

significantly reduced, leading to a less pronounced charge transfer. We also analyzed the distribution of electrons (green) and holes (blue) during the $D_0 \rightarrow D_1$ excitation process (Fig. 4a). For **Cz-BTM**, there is a substantial electron–hole separation with a distance of 2.418 Å. In contrast, **2PhN-BTM** and **2(2Cl(m)PhN)-BTM** exhibit more significant electron–hole overlap, indicating that their excitation processes are more characteristic of a localized excited (LE) state, with reduced electron–hole distances of 1.660 Å and 1.145 Å, respectively. The weakened CT characteristics are further corroborated by solvent effects (Fig. 4b). As solvent polarity increases from cyclohexane to dichloromethane, **Cz-BTM** exhibits a 40 nm red shift of its emission peak, indicating dominant CT characteristics, whereas **2PhN-BTM** and **2(2Cl(m)PhN)-BTM** exhibit smaller red shifts of only 22 nm and 11 nm, respectively, confirming their more pronounced LE characteristics.

Magnetic properties

The presence of unpaired electrons in luminescent radicals imparts unique paramagnetic properties. The magnetic behaviors of **2PhN-BTM** and **2(2Cl(m)PhN)-BTM** polycrystalline samples were investigated by using a superconducting quantum interference device (SQUID) magnetometer. Plots of mole magnetic susceptibility (χ_m) *versus T* for both radicals are presented in Fig. 5. Consistent with some reported luminescent radicals, χ_m of **2PhN-BTM** decreases rapidly with temperature increasing and follows the Curie–Weiss rule in the temperature range of 1.9 K to 300 K (Table S5†).[2,20,31–33] The Curie constant $C = 0.348$ emu mol^{-1} is close to the expected value for $S = 1/2$ spin systems without spin interactions (0.375 emu mol^{-1}), indicating dominant paramagnetic behavior in **2PhN-BTM**. Additionally, the small and negative Weiss temperature θ of **2PhN-BTM** (−3.7 K) suggests the presence of very week antiferromagnetic spin–spin interactions in the crystal.[31–33] This is likely due to the distorted molecular structure of luminescent triaryl methyl radicals, which limits strong intermolecular interactions such as $\pi\cdots\pi$ stacking.

In contrast, **2(2Cl(m)PhN)-BTM** exhibits a different magnetic behaviour. Upon cooling from 300 K, χ_m increases and reaches a maximum at around 13 K, followed by a decline as the temperature decreases further, indicating the occurrence of antiferromagnetic interactions.[34–38] The distinct trend near 13 K highlights obvious antiferromagnetic interactions in the **2(2Cl(m)PhN)-BTM** crystal at low temperature. When the temperature is below 7 K, χ_m increases sharply because of uncoupled radicals at crystal lattice defect sites.[35,38,39] The χ_m^{-1} *versus T* plot for **2(2Cl(m)PhN)-BTM** has good linearity between 22 K and 300 K and adheres to the Curie–Weiss rule (Fig. S8†).[34,35,38] Both the smaller $C = 0.339$ emu mol^{-1} and more negative $\theta = -16.2$ K compared to **2PhN-BTM** indicate stronger antiferromagnetic interactions in **2(2Cl(m)PhN)-BTM**. Furthermore, temperature-dependent magnetic susceptibility ($\chi_m T$) *versus T* for **2PhN-BTM** and **2(2Cl(m)PhN)-BTM** also reveals similar results, in which **2PhN-BTM** has a larger $\chi_m T$ value at room temperature than **2(2Cl(m)PhN)-BTM** (Fig. S9†). Despite the larger intermolecular central carbon atom distances of

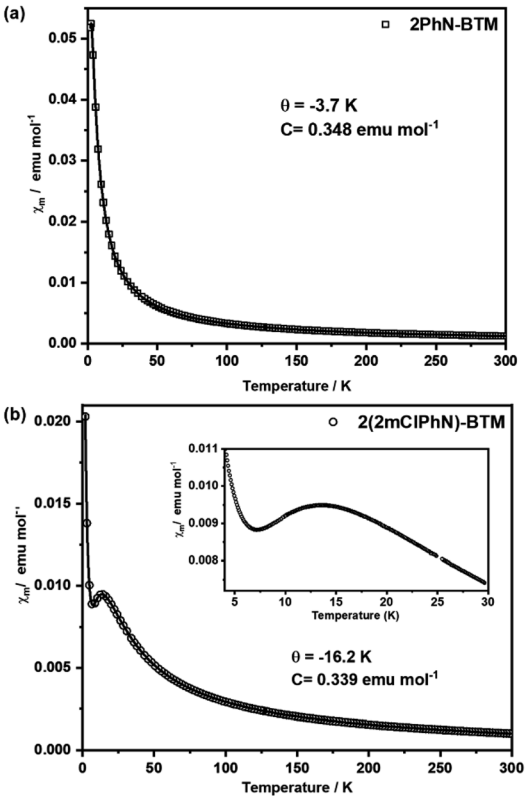

Fig. 5 Molar magnetic susceptibility (χ_m) *versus T* for (a) 2PhN-BTM and (b) 2(2Cl(m)PhN)-BTM at a temperature range of 1.9 K to 300 K.

2(2Cl(m)PhN)-BTM as shown in Fig. 1c, Cl$\cdots\pi$ halogen bonds between adjacent molecules enhance the intermolecular spin–spin interactions, contributing to the stronger antiferromagnetic behavior observed. Notably, this result marks the first observation of strong antiferromagnetic interaction characteristic of stable luminescent radicals, providing valuable insights into the interplay between molecular structure and magnetic behavior of organic luminescent radicals.

Conclusions

In summary, we successfully designed and synthesized stable diphenylamine BTM luminescent radicals, **2PhN-BTM** and **2(2Cl(m)PhN)-BTM**, which exhibit the rare α-type $D_0 \rightarrow D_1$ excitation while first maintaining D–A$^{\bullet}$ structure. Theoretical calculations suggest that the α-type transition is achieved by fine-tuning the energy levels of frontier orbitals and adjusting the relative values of the α and β energy gaps. This suggests that the conversion between α-type and β-type transition in luminescent radicals can be strategically controlled through molecular design. **2(2Cl(m)PhN)-BTM** demonstrated a significant increase in PLQY to 16% at 4 K. SQUID measurements revealed distinct magnetic properties between **2PhN-BTM** and **2(2Cl(m)PhN)-BTM**, which is attributed to the differences in their crystal structures. And, **2(2Cl(m)PhN)-BTM** is found to be the first luminescent radical that exhibits strong antiferromagnetic interactions in the crystal. Future research will focus on enhancing the room temperature PLQYs of diphenylamine

BTM radicals while preserving the α-type transition properties, and developing distinctive photophysical properties and application of α-type transition properties. This work presented a novel approach to designing α-type transition luminescent radicals.

Data availability

Data for this article, including synthetic procedures, details and characterization data, crystallographic data and calculation results, are available at DOI: **https://doi.org/10.1039/d4sc08026b**. The data supporting this article have been included as part of the ESI.† Crystallographic data for **2PhN-BTM** and **2(2Cl(m)PhN)-BTM** have been deposited at the Cambridge Crystallographic Data Centre (CCDC) under CCDC numbers: 2384400 and 2384389,† respectively.

Author contributions

Shengxiang Gao initiated the study, completed the experiments and analysis, and wrote the draft of the manuscript. Feng Li and Ming Zhang conceived and supervised the study, and reviewed and revised the manuscript. Chunxiao Wu provided experimental suggestions and participated in the data analysis.

Conflicts of interest

The authors declare no competing financial interests.

Acknowledgements

This work was financially supported by the National Natural Science Foundation of China (grant no. 51925303).

References

1 Q. Peng, A. Obolda, M. Zhang and F. Li, *Angew. Chem., Int. Ed.*, 2015, **54**, 7091–7095.
2 X. Ai, E. W. Evans, S. Dong, A. J. Gillett, H. Guo, Y. Chen, T. J. H. Hele, R. H. Friend and F. Li, *Nature*, 2018, **563**, 536–540.
3 F. Li, A. J. Gillett, Q. Gu, J. Ding, Z. Chen, T. J. H. Hele, W. K. Myers, R. H. Friend and E. W. Evans, *Nat. Commun.*, 2022, **13**, 2744.
4 H. H. Cho, S. Gorgon, H. C. Hung, J. Y. Huang, Y. R. Wu, F. Li, N. C. Greenham, E. W. Evans and R. H. Friend, *Adv. Mater.*, 2023, **35**, 2303666.
5 P. Murto, R. Chowdhury, S. Gorgon, E. Guo, W. Zeng, B. Li, Y. Sun, R. H. Friend and H. Bronstein, *Nat. Commun.*, 2023, **14**, 4147.
6 H.-H. Cho, S. Gorgon, G. Londi, S. Giannini, C. Cho, P. Ghosh, C. Tonnelé, D. Casanova, Y. Olivier, T. K. Baikie, F. Li, D. Beljonne, N. C. Greenham, R. H. Friend and E. W. Evans, *Nat. Photonics*, 2024, **18**, 905–912.
7 Q. Gu, S. Gorgon, A. S. Romanov, F. Li, R. H. Friend and E. W. Evans, *Adv. Mater.*, 2024, **36**, 2402790.
8 M. Ballester, J. Riera-Figueras, J. Castaner, C. Badfa and J. M. Monso, *J. Am. Chem. Soc.*, 1971, **93**, 2215–2225.
9 A. Heckmann, S. Dummler, J. Pauli, M. Margraf, J. Kohler, D. Stich, C. Lambert, I. Fischer and U. Resch-Genger, *J. Phys. Chem. C*, 2009, **113**, 20958–20966.
10 H. Guo, Q. Peng, X. K. Chen, Q. Gu, S. Dong, E. W. Evans, A. J. Gillett, X. Ai, M. Zhang, D. Credgington, V. Coropceanu, R. H. Friend, J. L. Bredas and F. Li, *Nat. Mater.*, 2019, **18**, 977–984.
11 J. Carilla, L. Fajari, L. Julia, J. Riera and L. Viadel, *Tetrahedron Lett.*, 1994, **35**, 6529–6532.
12 V. Gamero, D. Velasco, S. Latorre, F. Lopez-Calahorra, E. Brillas and L. Julia, *Tetrahedron Lett.*, 2006, **47**, 2305–2309.
13 D. Velasco, S. Castellanos, M. Lopez, F. Lopez-Calahorra, E. Brillas and L. Julia, *J. Org. Chem.*, 2007, **72**, 7523–7532.
14 S. Castellanos, D. Velasco, F. Lopez-Calahorra, E. Brillas and L. Julia, *J. Org. Chem.*, 2008, **73**, 3759–3767.
15 Y. Hattori, T. Kusamoto and H. Nishihara, *Angew. Chem., Int. Ed.*, 2014, **53**, 11845–11848.
16 S. Kimura, T. Kusamoto, S. Kimura, K. Kato, Y. Teki and H. Nishihara, *Angew. Chem., Int. Ed.*, 2018, **57**, 12711–12715.
17 K. Kato, S. Kimura, T. Kusamoto, H. Nishihara and Y. Teki, *Angew. Chem., Int. Ed.*, 2019, **58**, 2606–2611.
18 H.-H. Cho, S. Kimura, N. C. Greenham, Y. Tani, R. Matsuoka, H. Nishihara, R. H. Friend, T. Kusamoto and E. W. Evans, *Adv. Opt. Mater.*, 2022, **10**, 2200628.
19 X. Ai, Y. Chen, Y. Feng and F. Li, *Angew. Chem., Int. Ed.*, 2018, **57**, 2869–2873.
20 A. Abdurahman, Y. Chen, X. Ai, O. Ablikim, Y. Gao, S. Dong, B. Li, B. Yang, M. Zhang and F. Li, *J. Mater. Chem. C*, 2018, **6**, 11248–11254.
21 R. Matsuoka, A. Mizuno, T. Mibu and T. Kusamoto, *Coord. Chem. Rev.*, 2022, **467**, 214616.
22 S. Gao, Z. Cui and F. Li, *Chem. Soc. Rev.*, 2023, **52**, 2875–2885.
23 A. Mizuno, R. Matsuoka, T. Mibu and T. Kusamoto, *Chem. Rev.*, 2024, **124**, 1034–1121.
24 M. Ito, S. Shirai, Y. Xie, T. Kushida, N. Ando, H. Soutome, K. J. Fujimoto, T. Yanai, K. Tabata, Y. Miyata, H. Kita and S. Yamaguchi, *Angew. Chem., Int. Ed.*, 2022, **61**, e202201965.
25 T. Kushida, S. Shirai, N. Ando, T. Okamoto, H. Ishii, H. Matsui, M. Yamagishi, T. Uemura, J. Tsurumi, S. Watanabe, J. Takeya and S. Yamaguchi, *J. Am. Ceram. Soc.*, 2017, **139**, 14336–14339.
26 M. J. Frisch, G. W. Trucks, H. B. Schlegel, G. E. Scuseria, M. A. Robb, J. R. Cheeseman, G. Scalmani, V. Barone, B. Mennucci, G. A. Petersson, H. Nakatsuji, M. Caricato, X. Li, H. P. Hratchian, A. F. Izmaylov, J. Bloino, G. Zheng, J. L. Sonnenberg, M. Hada, M. Ehara, K. Toyota, R. Fukuda, J. Hasegawa, M. Ishida, T. Nakajima, Y. Honda, O. Kitao, H. Nakai, T. Vreven, J. A. Montgomery, J. E. Peralta, F. Ogliaro, M. Bearpark, J. J. Heyd, E. Brothers, K. N. Kudin, V. N. Staroverov, T. Keith, R. Kobayashi, J. Normand, K. Raghavachari, A. Rendell, J. C. Burant, S. S. Iyengar, J. Tomasi, M. Cossi, N. Rega, J. M. Millam, M. Klene, J. E. Knox, J. B. Cross, V. Bakken, C. Adamo, J. Jaramillo, R. Gomperts, R. E. Stratmann, O. Yazyev, A. J. Austin, R. Cammi, C. Pomelli,

J. W. Ochterski, R. L. Martin, K. Morokuma, V. G. Zakrzewski, G. A. Voth, P. Salvador, J. J. Dannenberg, S. Dapprich, A. D. Daniels, O. Farkas, J. B. Foresman, J. V. Ortiz, J. Cioslowski and D. J. Fox, *Gaussian 09 (Revision D.01)*, Gaussian, Inc., Wallingford CT, 2013.

27 T. Lu and F. Chen, *J. Comput. Chem.*, 2012, **33**, 580–592.

28 Z. Liu, T. Lu and Q. Chen, *Carbon*, 2020, **165**, 461–467.

29 M. A. Fox, E. Gaillard and C. C. Chen, *J. Am. Chem. Soc.*, 1987, **109**, 7088–7094.

30 S. R. Ruberu and M. A. Fox, *J. Phys. Chem.*, 1993, **97**, 143–149.

31 Y. Ogino, T. Kusamoto, Y. Hattori, M. Shimada, M. Tsuchiya, Y. Yamanoi, E. Nishibori, K. Sugimoto and H. Nishihara, *Inorg. Chem.*, 2017, **56**, 3909–3915.

32 R. Matsuoka, S. Kimura and T. Kusamoto, *ChemPhotoChem*, 2021, **5**, 669–673.

33 S. Kimura, R. Matsuoka, S. Kimura, H. Nishihara and T. Kusamoto, *J. Am. Chem. Soc.*, 2021, **143**, 5610–5615.

34 S. Aboaku, A. Paduan-Filho, V. Bindilatti, N. F. Oliveira, J. A. Schlueter and P. M. Lahti, *Chem. Mater.*, 2011, **23**, 4844–4856.

35 C. P. Constantinides, A. A. Berezin, M. Manoli, G. M. Leitus, G. A. Zissimou, M. Bendikov, J. M. Rawson and P. A. Koutentis, *Chem.–Eur. J.*, 2014, **20**, 5388–5396.

36 A. Gardias, P. Kaszyński, E. Obijalska, D. Trzybiński, S. Domagała, K. Woźniak and J. Szczytko, *Chem.–Eur. J.*, 2018, **24**, 1317–1329.

37 Y. Takahashi, R. Matsuhashi, Y. Miura and N. Yoshioka, *Chem.–Eur. J.*, 2018, **24**, 7939–7948.

38 Z. Liang, Y. Tan, S. N. Hsu, J. F. Stoehr, H. Tahir, A. B. Woeppel, S. Debnath, M. Zeller, L. Dou, B. M. Savoie and B. W. Boudouris, *Mol. Syst. Des. Eng.*, 2023, **8**, 464–472.

39 S. Kapurwan, A. Gupta, A. Mondal and S. Konar, *ChemistrySelect*, 2022, **7**, e202104536.